Suppression of Time-Varying Interharmonics Produced by Medium-Frequency Induction Melting Furnaces by a HAPF System

Emre Durna, *Student Member, IEEE*, İlker Yılmaz, *Student Member, IEEE*,
and Muammer Ermiş, *Senior Member, IEEE*

***Abstract*—This paper describes the design and field implementation of a hybrid active power filter (HAPF) system to suppress time-varying interharmonics injected into the grid by medium-frequency coreless induction melting furnaces (IMFs). In a sample steel melt shop, variable-frequency load-resonant inverters of works coils are supplied from the medium-voltage grid via 12- and 24-pulse thyristor rectifiers. The cross-modulation phenomenon in ac–dc–ac link of the medium-frequency coreless IMF installations produces interharmonics and characteristic and uncharacteristic harmonics in the grid-side line current waveforms. Furthermore, frequencies of dominant interharmonics are migrating in time inside a frequency window as the operating frequency of the load-resonant inverter varies in wide range during a melting cycle. The HAPF system developed for this application consists of nine HAPF units operating in parallel in current control mode and is connected to the grid via a coupling transformer. Current control is achieved by extracting high-order fixed frequency characteristic harmonic components from the reference current signal and defining a fixed hysteresis band for each HAPF unit. The input *LC* filter of the HAPF system is optimized in the design stage by taking into account the frequency range of prominent interharmonics. Theoretical findings are verified in a sample steel melt shop by extensive field measurements. Field test results have shown that the developed HAPF system suppresses successfully the dominant time-varying interharmonics and harmonics in the frequency range from 250 to 650 Hz.**

***Index Terms*—Harmonics, hybrid active power filter, hysteresis current control, induction melting furnace, interharmonics.**

I. INTRODUCTION

OVER the last two decades, medium-frequency coreless induction melting furnaces (IMFs) have been used increasingly in small/medium-size steel melt shops and alloy steel plants due to their competitive installation costs and relatively low running costs. The operating power and frequency of medium-frequency coreless IMFs are in the ranges of 10 kW to 32 MW and 150–250 Hz, respectively, up to 60 t capacity. In a high-power-density IMF, the work coil is fed from a single-phase solid-state inverter operating at medium frequency. Load-resonant thyristor or IGBT inverters have been designed to allow the output power frequency to change during a melting cycle in order to maintain tuning to the natural frequency of the work coil [1]–[3]. This way, electrical power input to the IMF installation is nearly kept constant over a melting period. The dc link of the load-resonant inverter is usually fed from a multipulse (12-pulse or 24-pulse) thyristor rectifier due to its lower capital cost, especially if the installed capacity of the IMF installation is relatively high.

The cross-modulation phenomenon in ac–dc–ac link of medium-frequency coreless IMF installations having thyristor converters produces interharmonics and characteristic and uncharacteristic harmonics in the supply-side line current waveforms [4]–[6]. Furthermore, interharmonic frequencies are changing in time as the operating frequency of the load-resonant inverter varies in a wide range in a melting cycle, as reported in [4] in detail. Interharmonic current components injected into the power system may interact with conventional reactive power compensation systems consisting of shunt harmonic filters tuned to characteristic power system harmonics [7], resulting in destructive effects on reactive power compensation equipment, malfunctioning of protection relays, and production of pulsating and braking torque in rotating electrical machines [8].

Some researchers have recommended the use of active power filters (APFs) to suppress interharmonic current components of medium-frequency IMF by considering the drawbacks of passive shunt harmonic filter solutions [6], [9], [10]. In [11] and [12], IMF harmonics are compensated respectively by a static synchronous compensator (STATCOM) and a hybrid active power filter (HAPF) without addressing interharmonics.

Various active filter topologies and their use in industry applications have been reviewed in [13]. It has been shown in [14] by computer simulations that a HAPF has some advantages such as lower dc-link voltage, higher efficiency, less switching ripple, and lower EMI emission in comparison with those of the equivalent shunt APF. There are different circuit topologies and control methods for HAPF systems as recorded in the literature [10], [15]–[19]. In [10], a HAPF consisting of a shunt tuned *LC* filter connected in series with an APF via a coupling transformer has been considered for suppression of constant frequency interharmonic currents. Design of a transformerless

---

Manuscript received November 22, 2015; accepted March 9, 2016. Date of publication March 15, 2016; date of current version November 11, 2016. Recommended for publication by Associate Editor Friedrich W. Fuchs.

E. Durna is with the Department of Electrical and Electronics Engineering, Orta Doğu Teknik Üniversitesi, Ankara 06800, Turkey (e-mail: emredurna@gmail.com).

İ. Yılmaz is with the Department of Electrical and Electronics Engineering, Orta Doğu Teknik Üniversitesi, Ankara 06800, Turkey (e-mail: ilker.yilmaz@basarienerji.com).

M. Ermiş is with the Department of Electrical and Electronics Engineering, Orta Doğu Teknik Üniversitesi, Ankara 06800, Turkey (e-mail: ermis@metu.edu.tr).

Color versions of one or more of the figures in this paper are available online at http://ieeexplore.ieee.org.

Digital Object Identifier 10.1109/TPEL.2016.2542140

HAPF consisting of a tuned *LC* filter connected in series with an APF has been presented in [16]. Different dc voltage control strategies in a three-phase four-wire HAPF have been investigated in [19] for dynamic reactive power compensation. A transformerless HAPF, which consists of a passive *LC* filter tuned to the seventh harmonic frequency and connected in series with an APF, is integrated into a medium-voltage (MV) motor drive in [15] to mitigate harmonics in the line current waveforms on the supply side. A nonlinear control technique has been recommended in [18] for a transformerless HAPF. In [10] and [15]–[19], only the suppression of characteristic power system harmonics has been considered. In most of the HAPF systems either the *K* control strategy [10], [15], [16] or the hysteresis band control [17], [19] has been used.

Hysteresis band control has been considered as an effective current control method in various industrial systems such as variable-frequency motor drives [20]–[23], APFs [24]–[28], HAPFs [17], [29], dynamic voltage restorer [30], the static compensator [31], etc. The fundamental method for the implementation of hysteresis band control is the use of a fixed hysteresis band as described in [25], [29], [31], and [32]. However, the choice of a fixed band may cause the switching frequency to vary in a wide range. Some researchers used adaptive bands to fix the switching frequency at an optimum value for the chosen power semiconductors [23], [26], [30], [33]. Some other approaches have also been recommended in the literature [21], [22], [32], [34] for the implementation of hysteresis band control. Hysteresis band control has been implemented in [21], by using space vector modulation pulsewidth-modulated (PWM) technique. Sinusoidal and parabolic hysteresis band variations have been recommended in [22] and [34], respectively. A different current control method has been proposed in [32] for single-phase grid-connected inverters to track the reference current signal at constant switching frequency without defining a hysteresis band. All papers mentioned earlier do not deal with time-varying interharmonic frequencies in the application of hysteresis band control.

In this study, the time-varying dominant interharmonic and harmonic current components injected into the grid by 12- and 24-pulse IMFs operating in a sample steel melt shop are significantly reduced by a HAPF system. These dominant interharmonic frequencies are changing in time from 250 to 550 Hz, as the operating frequency of load-resonant H-bridge inverter in Fig. 1varies in a considerable range from 150 to 250 Hz within the melting cycle. This paper describes for the first time the design, implementation, and performance of a HAPF system with hysteresis current control in order to suppress those migrating interharmonics. The input *LC* filter is optimized in the design stage by considering the frequency range of dominant interharmonics and technical requirements for the HAPF converters and the sample steel melt shop. High-order characteristic harmonic components injected by the IMF installations are extracted from the reference current signal in order to avoid undesirably high switching frequencies and operating dc-link voltages for the HAPF converters. A fixed but an optimum hysteresis band has been specified to track the resulting reference current signal. Field test results have shown that the developed HAPF system suppresses successfully the dominant time-varying interharmonics and harmonics.

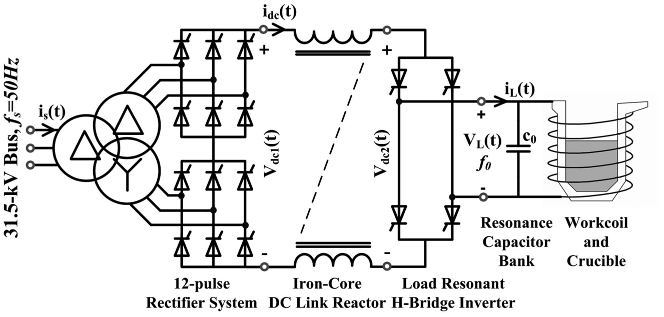

Fig. 1. Simplified power circuit diagram of a typical medium-frequency coreless IMF.

II. Problem Definition

Circuit diagram of a typical medium-frequency coreless induction steel melting furnace installation is given in Fig. 1. Most of the steel melt shops are furnished with more than one furnace having 12- and/or 24-pulse thyristor-controlled rectifier circuits on the supply side.

A medium-frequency coreless IMF installation is one of the most problematic loads in the power system from the viewpoint of interharmonics. This is because such an installation produces interharmonic and uncharacteristic harmonic current components in a wide frequency range owing to cross-modulation phenomenon across the ac–dc–ac link of the multipulse rectifier and current-fed load-resonant inverter cascade. [4] These interharmonic current components are migrating in time inside a frequency window, e.g., from 250 to 550 Hz, as the operating frequency of load-resonant H-bridge inverter in Fig. 1 varies in a considerable range from 150 to 250 Hz, within the melting cycle.

Frequencies of interharmonic current components f_{ih} in the MV supply lines in Fig. 1 are given by

$$f_{\text{ih}} = (1 \pm nP)\, f_s \pm 2k f_o(t) \tag{1}$$

where *P* is the pulse number of the rectifier circuit, $f_s = 50$ Hz is the supply frequency, f_o is the operating frequency of the load-resonant H-bridge inverter, index $n = 0, 1, 2, 3, \ldots$, and index $k = 1, 2, 3, \ldots$

Furthermore, multipulse rectifier circuits on the supply-side produce their own characteristic current harmonic components. Frequencies of characteristic harmonics f_h produced by three-phase rectifiers can be computed as follows:

$$f_h = (1 \pm nP)\, f_s. \tag{2}$$

As an example, a 12-pulse thyristor rectifier produces 11th, 13th, 23rd, 25th, . . . , characteristic current harmonics, whereas a 24-pulse thyristor rectifier is producing 23rd, 25th, 47th, 49th, . . . , harmonics. A negative frequency value found from (1) or (2) should be considered as a negative-sequence interharmonic or harmonic current component, whereas a positive-frequency value as a positive-sequence component. Variations

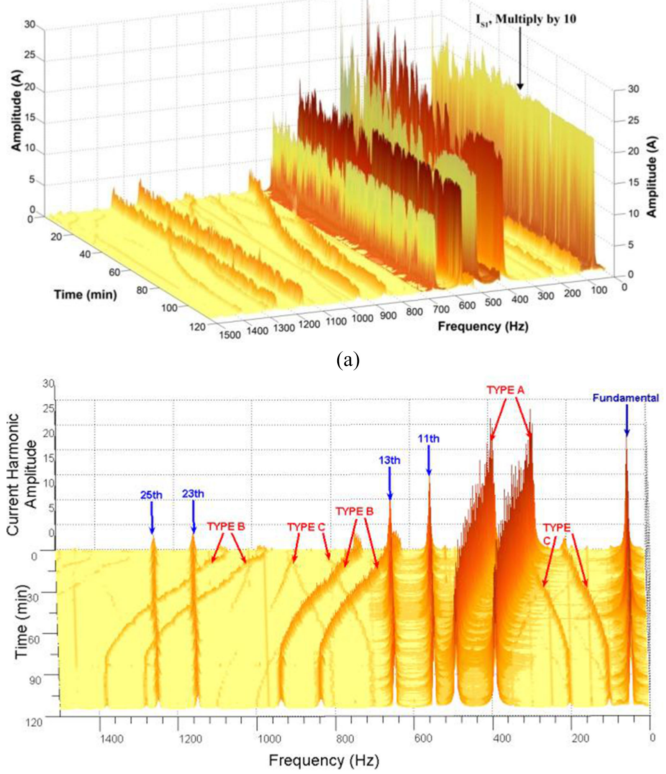

(a)

(b)

Fig. 2 Variations in supply-side line current interharmonics and harmonics for a 12-pulse IMF installation during a typical melting cycle (deduced from the data recorded in the field) [4]. Type A: Interharmonics due to the cross modulation of fundamental supply frequency f_s and the inverter output fundamental frequency referred to the dc link $2f_o$, where $f_{\rm cr} = 2f_o \pm f_s$. Type B: The cross modulation of f_s with current harmonic frequencies at the dc link at $2kf_o$, with $k = 2, 3, \ldots$, where $f_{\rm cr} = 2kf_o \pm f_s$. Type C: The cross modulation of supply harmonic current frequencies at $(1 \pm 12n)f_s$, for $n = 1, 2, 3, \ldots$, and the dc-link current harmonic frequency at $2f_o$, where $f_{\rm cr} = (1 \pm 12n)f_s \pm 2f_o$.

TABLE I
POWER SYSTEM HARMONICS

Three-Phase Sinusoidal Current Systems	Characteristic Harmonics	Uncharacteristic Harmonics
Positive sequence	1st, 7th, 13th, 19th, …	4th, 10th, 16th, 22nd, …
Negative sequence	5th, 11th, 17th, 23rd, …	2nd, 8th, 14th, 20th, …
Zero sequence	3rd, 9th, 15th, 21st, …	6th, 12th, 18th, 24th, …

in the supply-side line current interharmonics and harmonics of a 12-pulse medium-frequency IMF installation for a typical melting cycle are as shown in Fig. 2 [4]. These variations have been deduced from the raw data collected by the monitoring device in [35], sampled at a rate of 12.8 kS/s/channel on the supply side, via postprocessing by fast Fourier transform (FFT) tool of MATLAB using ten-cycle windows in order to achieve a 5-Hz frequency resolution, as recommended in [36].

Characteristic current harmonics in power systems [37], frequencies of which are odd integer multiples of supply frequency, can be characterized as given in Table I. On the other hand, nonlinear loads such as arc and ladle furnaces, and etc. also produce uncharacteristic even-order power system harmonics given in Table I. These positive-, negative-, and zero-sequence current components are the characteristics of power system elements such as rotating electrical machines, transformers, and line-commutated converters in which current harmonic components are synthesized with respect to the fundamental component ($f_1 = f_s = 50\,\mathrm{Hz}$) of supply voltages and currents. However, this is not the case for power system components causing cross-modulation phenomenon.

Since medium-frequency IMF installation is a three- phase, three-wire system, there will be no zero-sequence current components in the supply lines. An IMF can therefore be classified as a balanced ($i_A(t) + i_B(t) + i_C(t) = 0$) and symmetrical three-phase load by considering only the fundamental components of current and voltages. This classification is consistent with the one in [37]. In the supply line current waveforms of an IMF installation, all harmonics and all interharmonic frequencies are present in a typical melting cycle as can be understood from Fig. 2 and (1) and (2). However, any interharmonic or harmonic current component will appear either as a positive- or negative-sequence component at any instant of melting process. On the other hand, for a steel melt shop having more than one IMF installations, positive- and negative-sequence components of any interharmonic or harmonic frequency may be present at any instant in the line current waveforms on the supply side. From this viewpoint, such a steel melt shop, before suppression of interharmonics and harmonics, can be considered as a balanced but asymmetrical three-phase system.

The traditional approach for the solution of reactive power compensation and/or harmonic filtering problems in industrial plants is the use of shunt plain capacitor banks and/or filter banks usually tuned to characteristic power system odd-order harmonic components. Some of the passive shunt filter banks in static var compensation systems of electric arc and ladle furnace installations are tuned to uncharacteristic even-order power system harmonics. Interharmonics injected into the power system by a medium-frequency IMF may interact with the passive shunt harmonic filters of the nearby industrial plants or those supplied from the point of common coupling (PCC), thereby causing overvoltages and/or overload currents owing to the amplification of those interharmonics or resonances. These interharmonics may also cause misoperation of protection relays and production of braking torques in rotating electrical machines. In this study, interharmonic and harmonic current components injected by a medium size steel melt shop containing three IMF installations are satisfactorily suppressed by using a HAPF system with hysteresis band control.

III. SYSTEM DESCRIPTION AND DESIGN

Single-line diagram of the sample steel melt shop to which the HAPF system has been installed is as shown in Fig. 3. The steel melt shop has two 12-pulse and one 24-pulse IMF installations each rated at 12 MVA and supplied from a 50-Hz, 31.5-kV MV bus. The primary objective of this study is to design a flexible and modular HAPF system to meet the requirements of various steel melt shops having different number of IMF installations

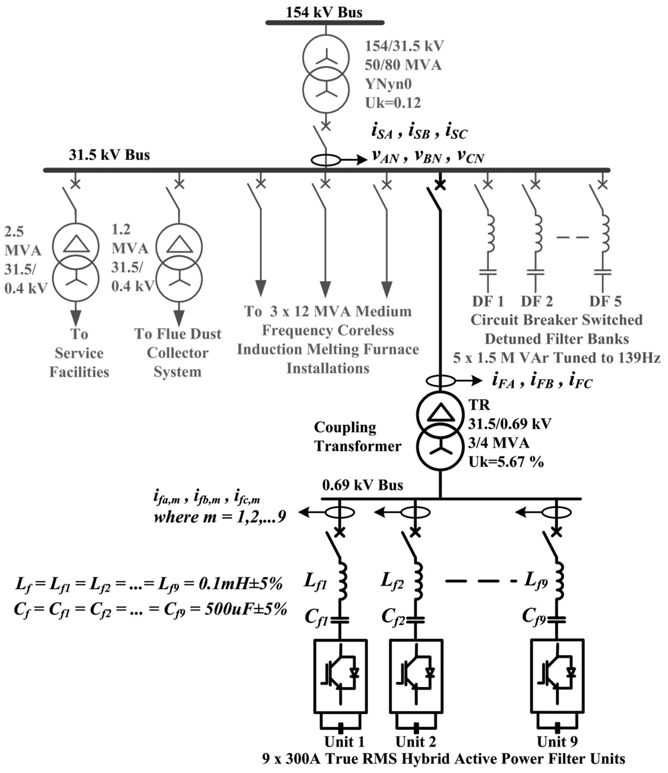

Fig. 3 Single-line diagram of sample steel melt shop.

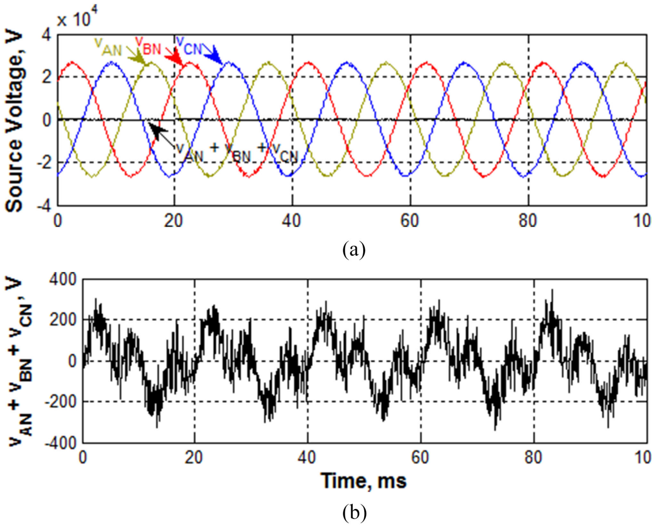

Fig. 4 Grid voltages recorded in the field (a) line-to-neutral voltage waveforms (accuracy class: 1.0, voltage ratio error: ±1.0%) and (b) sum of instantaneous values of line-to-neutral voltages.

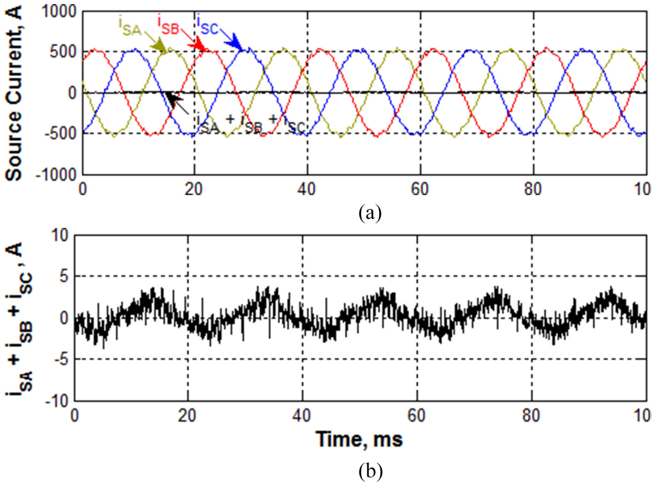

Fig. 5 Currents drawn by the sample steel melt shop containing HAPF system from the grid (recorded in the field) (a) line current waveforms (accuracy class: 5P, current ratio error: ±1%) and (b) sum of the instantaneous line currents.

and different grid voltage levels. This is achieved by designing a standardized 300 A true RMS HAPF converter operating connected to 690 V bus via $L_f C_f$ series filter as the building block of the HAPF system. Several identical HAPF units can then be operated in parallel to meet interharmonic compensation requirements of any steel melt shop. In the sample melt shop, nine identical HAPF units are connected to the 31.5-kV bus via a specially designed coupling transformer. In the case where the flexible and modular HAPF system is going to be applied to another steel melt shop, the number of HAPF units, technical specifications of the coupling transformer, and/or $L_f C_f$ values may need to be revised. On the other hand, reactive power demand of the plant is compensated by five circuit breaker switched detuned filter banks as shown in Fig. 3.

In order to prove that the sample steel melt shop is a three-phase, three-wire balanced system, supply-side line-to-neutral voltages ($v_{\mathrm{AN},} v_{\mathrm{BN},} v_{\mathrm{CN}}$) and line currents ($i_{\mathrm{SA},} i_{\mathrm{SB},} i_{\mathrm{SC}}$) in Fig. 3 are recorded by using the multipurpose platform in [35] operated in raw data collection mode. Figs. 4 and 5 show some sample records. As can be understood from Figs. 4(b) and 5(b), $v_{\mathrm{AN}} + v_{\mathrm{BN}} + v_{\mathrm{CN}} \approx 0$ (less than 1% of the line-to-neutral voltages), and $i_{\mathrm{SA}} + i_{\mathrm{SB}} + i_{\mathrm{SC}} \approx 0$ (less than 1% of the line currents), respectively. Line current waveforms of all loads in the sample steel melt shop in Fig. 6 are also deduced from the sampled data when two 12-pulse IMF installations are in operation. Fig. 6(b) shows that $i_{\mathrm{LA}} + i_{\mathrm{LB}} + i_{\mathrm{LC}} \approx 0$ (less than or equal to 1% of the load currents). Summation of line-to-neutral voltages and line currents in Figs. 4(b), 5(b), and Fig. 6(b) are mainly attributed to the measurement errors of conventional voltage and current transformers. Furthermore, the symmetrical components of load current harmonics and interharmonics with 5 Hz frequency resolution are determined by applying the three-phase symmetrical-component transformation to the postprocessed load current data by FFT tool of MATLAB using ten-cycle windows. Some sample results for $f_1 = 50$ Hz, $f_h = 350$ Hz, and $f_{\mathrm{ih}} = 435$ Hz are as shown in Fig. 7(a), (b), and (c), respectively. It is worth to note that the seventh harmonic current component would be a positive-sequence quantity in conventional power system applications. However, in this application, the dominant component of the seventh harmonic current mostly appears as the negative sequence component, as illustrated in Fig. 7(b). On the other hand, positive-sequence component at $f_{\mathrm{ih}} = 435$ Hz in Fig. 7(c) is produced by one of the IMF installations while the negative-sequence component

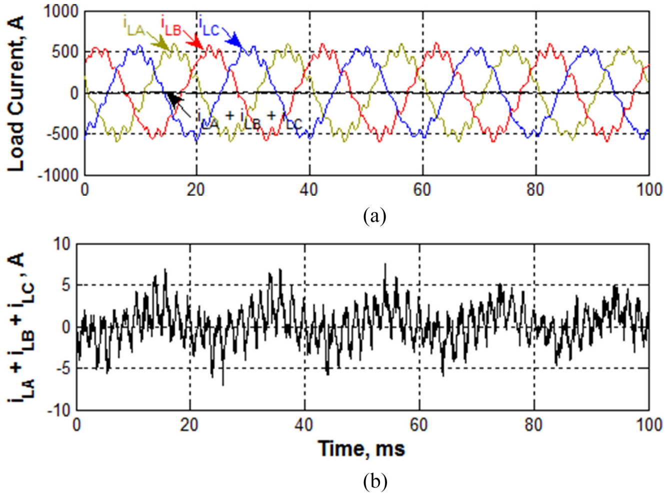

Fig. 6 Currents consumed by all loads in the sample steel melt shop by subtracting HAPF system current waveform from the supply current waveform: both recorded in the field (HAPF system CTs: 0.5 s accuracy class) (a) line current waveforms and (b) sum of the instantaneous line currents.

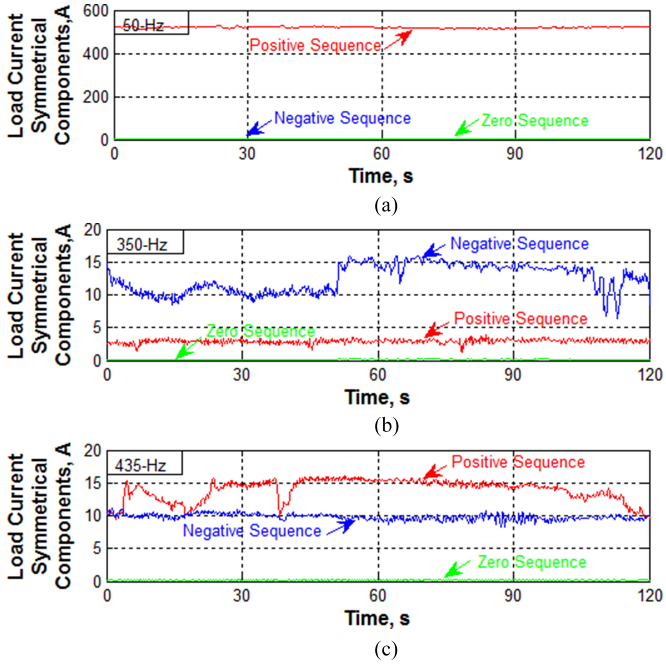

Fig. 7 Sequence components of some sample harmonic and interharmonic load current components (a) $f_1 = 50$ Hz, (b) $f_h = 350$ Hz, and (c) $f_{\text{ih}} = 435$ Hz.

by the other. Positive and negative sequences of an interharmonic can also be produced by one of the IMFs; for this case, the magnitude of one of the sequence components will be much smaller than the other. For example, when $f_o = 175\,\text{Hz}$ and $p = 12$, $k = 1$ and $n = 0$ gives $f_{\text{ih}} = -300\,\text{Hz}$, while $k = 1$ and $n = 1$ give $f_{\text{ih}} = +300\,\text{Hz}$ using (1). Note that the negative sequence component is much larger than the positive-sequence component, as illustrated in Fig. 2, respectively, by Type A and Type C interharmonics, which are crossing at 300 Hz.

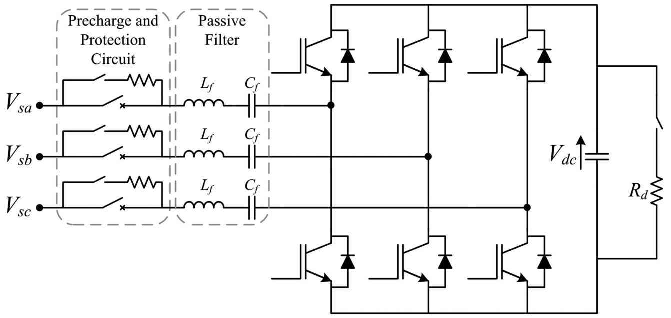

Fig. 8 Three-phase, three-wire, two-level VSC-type HAPF unit.

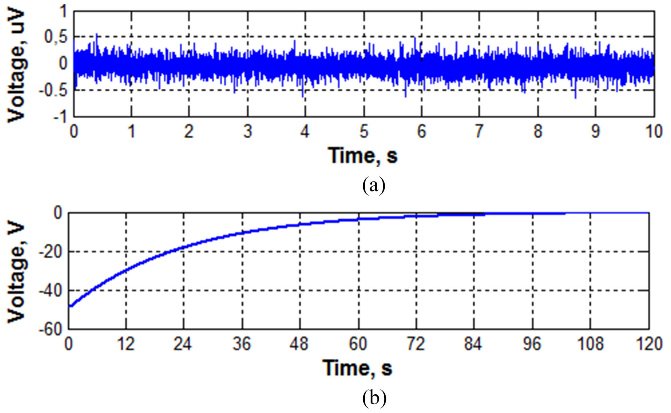

Fig. 9 Sum of VSC converter voltages with respect to neutral point of the coupling transformer secondary when filter capacitors before energization are (a) fully discharged and (b) partially discharged (PSCAD simulation).

In this application, in order to reduce the dc-link voltage rating and hence power semiconductor ratings, the HAPF topology shown in Fig. 8 is chosen. Each HAPF unit contains a series $L_f C_f$ filter between coupling transformers' secondary terminals and ac terminals of three-phase, three-wire, two-level voltage-source-converter (VSC) type HAPF converter in order to block fundamental component of bus voltage.

A. Design of Input LC Filter

Since the loads in steel melt shop are balanced, three-phase, three-wire VSC-type HAPF converters in Fig. 3 can be modeled with respect to the neutral point of the coupling transformer secondary. This is proven by a detailed EMTDC/PSCAD simulation of the overall system in Fig. 3 by calculating the sum of converter voltages with respect to the coupling transformer neutral point ($\Sigma v_{\text{fx}-n} = v_{\text{fa}-n} + v_{\text{fb}-n} + v_{\text{fc}-n}$), from the actual load current data obtained in the field and by operating the HAPF system according to the control philosophy described in this paper. In the implemented system, input filter capacitors C_f are equipped with parallel connected discharge resistors to discharge the capacitors nearly in 2 min time whenever the HAPF units are de-energized. This means that filter capacitors are usually fully discharged before reconnecting the associated HAPF units to the secondary of the coupling transformer. Fig. 9(a) shows the variations in $\Sigma v_{\text{fx}-n} = v_{\text{fa}-n} + v_{\text{fb}-n} + v_{\text{fc}-n}$ by assuming that

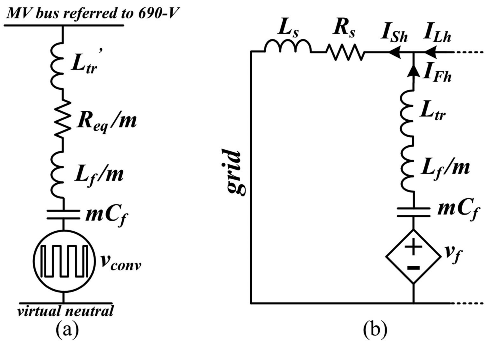

(a) (b)

Fig. 10 HAPF system referred to the LV side of the coupling transformer (a) single-line diagram and (b) per-phase interharmonic/harmonic equivalent circuit.

initially all the filter capacitors are fully discharged. If the filter capacitors were not fully discharged before energizing the HAPF units, the variations in $\Sigma v_{\mathrm{fx}-n} = v_{\mathrm{fa}-n} + v_{\mathrm{fb}-n} + v_{\mathrm{fc}-n}$ would be as in Fig. 9(b). Therefore, per-phase equivalent circuit of each VSC converter can be obtained with respect to the neutral point of the coupling transformer secondary.

Fig. 10 shows the equivalent single-line diagram and the corresponding harmonic equivalent circuit of the HAPF system referred to the low voltage (LV) side of the coupling transformer, where v_{conv} is the equivalent ac voltage of the VSC converters, m the number of identical HAPF units operated simultaneously ($m = 9$ for this particular application), L'_{tr} the total leakage inductance of the coupling transformer referred to the LV side, L_f the self-inductance of each iron-core filter reactor, and C_f is the capacitance of each power electronics type filter capacitor. For the sake of simplicity in the analysis, internal resistances of transformer and filter reactors are neglected in Fig. 10.

In the sample steel melt shop application presented in this paper, the input *LC* filter is tuned to 385 Hz for $m = 9$. This is because prominent interharmonics appear in the frequency range from 250 to 550 Hz and nine simultaneously operated HAPF units give the most effective filtering performance. Since the tuning frequency w_o of the input *LC* filter is given by (3) and L'_{tr} is assumed to be fixed, infinitely many (L_f, C_f) pairs satisfy it

$$w_o = 1/\sqrt{LC} = 2\pi 385\,\mathrm{rad/s}. \tag{3}$$

where $L = L'_{\mathrm{tr}} + L_f/m, C = mC_f$, and $m = 9$.

Optimum values of L_f and C_f are determined in view of following requirements.

1) DC-link voltage of the VSC converter should be kept at a reasonably low value, and
2) The HAPF system should supply sufficient amount of reactive power to compensate for reactive power demand of plant transformers when the plant is idle in the third shift. This is measured to be 700 kvar at the rated voltage.

The impedance characteristics are given in Fig. 11 as a function of $L = L'_{\mathrm{tr}} + L_f/9$. The following conclusions can be drawn from these characteristics:

1) Input *LC* filter is tuned to 385 Hz in order to suppress interharmonics effectively not only in the range above but also below the tuning frequency. The optimum value of the tuning frequency is not fixed to 400 Hz, midway between 250 and 550 Hz. This is because, magnitudes of filter impedance in resistive–capacitive region are relatively higher than those of resistive–inductive region. That is why the tuning frequency in the design process has been moved by 15 Hz toward the minimum frequency.
2) VSC-type HAPF converters in Fig. 3 are going to be operated in current control mode according to the philosophy of hysteresis band control. Therefore, equivalent impedance of the input *LC* filter against a dominant interharmonic frequency or frequency band dictates the magnitude of v_{conv} at these interharmonic frequencies. A higher value for v_{conv} requires a higher dc-link voltage for the HAPF converters thus violating the idea behind the choice of the HAPF topology. Therefore, the input impedance of the series *LC* filter should be kept at a reasonably low value in the design phase against the frequencies corresponding to dominant interharmonics.

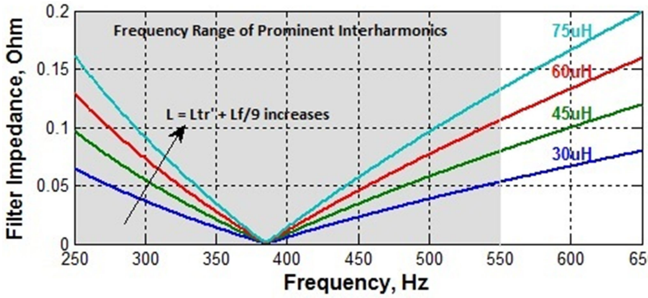

Fig. 11 Impedance characteristics of the input *LC* filter for the HAPF system.

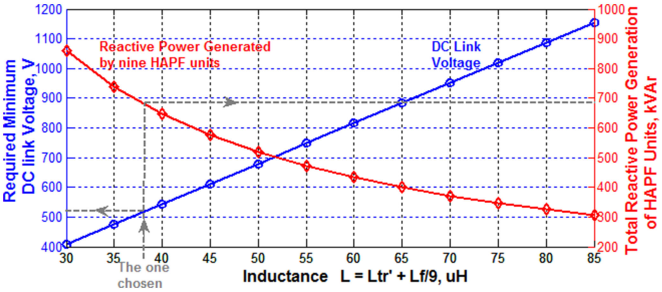

Fig. 12 Optimization of the series filter inductance *L* for the HAPF system.

In order to be able to determine the optimum value of *L* and hence L_f, the variations in total reactive power generated by nine parallel-operated HAPF units (excluding coupling transformer) and minimum value of the required dc-link voltage are calculated as a function of *L* and then plotted on a common graph as shown in Fig. 12. 50 Hz component of v_{conv} is very low (in the implemented system, less than 3% of 690 V transformer secondary voltage) in comparison with the voltage rating of HAPF units. This 50 Hz component is needed to allow active power flow from utility grid to HAPF converters in order to compensate for converter losses. Almost all of the 50 Hz bus voltage will then appear across the terminals of *LC* filter. This means that the VSC-type HAPF converter provides nearly a short circuit path to 50 Hz current components flowing in the lines of series *LC* filter. Therefore, total reactive power generation of HAPF units in Fig. 12, is easily calculated by considering only the 50 Hz component. For the calculation of minimum value of the required dc-link voltage of VSC converters, current data recorded in the field for nearly 200 min time period, while three IMFs are in operation, are examined carefully, and then dominant interharmonic components and their magnitudes are determined. For each dominant interharmonic component, corresponding potential drop on the input *LC* filter is calculated by using filter impedance characteristics in Fig. 11 as a function of *L*. Peak value of V_f component of each dominant interharmonics is then determined by using the harmonic equivalent circuit in Fig. 10(b). These peak values are then added algebraically in order to give us minimum value of the required dc-link voltage $V_{\mathrm{dc(min)}}$, by assuming that in the worst case their peak values are coincident [38]. This MATLAB analysis yields $V_{\mathrm{dc(min)}}$ versus *L* characteristic in Fig. 12. In view of the requirements in 1) and 2) defined previously, and by using the characteristics in Fig. 12, the optimum values of C_f, *L,* and hence L_f are chosen to be 500 μF, 38 μH, and 0.1 mH, respectively.

B. Hysteresis Band Control of HAPF

Basic philosophy in the design of the HAPF system is to suppress interharmonic and harmonic current components injected by IMFs, instead of eliminating them. This will be achieved by operating the HAPF system in current control mode by using the hysteresis band control method. Each HAPF unit has its own controller, as shown in Fig. 13. All of these nine controllers, one for each HAPF unit, receive the same sampled input data which are the grid-side line currents ($i_{\mathrm{SA}}, i_{\mathrm{SB}}, i_{\mathrm{SC}}$), line currents of the HAPF system on the grid side of the coupling transformer ($i_{\mathrm{FA}}, i_{\mathrm{FB}}, i_{\mathrm{FC}}$), and line to neutral grid voltages (v_{AN} and v_{BN}) to generate PLL signals. For this purpose, line current waveforms of the grid and HAPF system and line-to-neutral grid voltages are simultaneously sampled at a rate of 25-kS/s per channel via the DSP board (TI, TMS320F28335). Since three IMF installations are in operation in the sample steel melt shop, line current waveforms of all loads are indirectly determined by subtracting synchronously the current samples of the HAPF system from the source current samples.

The digital controller in Fig. 13 is composed of interharmonic and harmonic current reference generation, selective harmonic extraction, dc-link regulation, 50 Hz current reference generation for input *LC* filter, PLL signal generation, and hysteresis band controller blocks. Load currents ($i_{\mathrm{LA}}, i_{\mathrm{LB}}, i_{\mathrm{LC}}$), obtained from the source and HAPF currents, sampled on the MV side, are converted to LV side of the system ($i_{\mathrm{la}}, i_{\mathrm{lb}}, i_{\mathrm{lc}}$) by using Δ/Y and turns-ratio transformations. These currents in *abc* reference frame are then transformed to $\alpha\beta0$ reference frame by using the well-known three-phase to two-phase transformation. Since the plant constitute a balanced but asymmetrical three-phase system, i_o component in all computation steps is taken to be zero. On the other hand, 23rd and 25th characteristic current harmonics produced by 12- and 24-pulse rectifier circuits are removed from the reference current signal by the selective harmonic extraction block in order to prevent HAPF units from being overloaded. This is because, since the impedance of the input *LC* filter is very high at such high-order characteristic harmonics, a dc-link voltage higher than the design value would be needed. Fundamental components of the line current waveforms are also extracted from the resulting reference current signals described earlier by using $\alpha\beta0$ to dq0 transformation matrix and low-pass filters (LPF) as shown in the interharmonic and harmonic current reference block in Fig. 13.

G in the block diagram of the controller is set to a value less than 1/9 for considerable reduction of interharmonic and harmonic current components instead of elimination. The *q*-axis component of the reference current signal is combined with a constant 50 Hz current reference (50 Hz bus bar voltage divided by 50 Hz filter impedance) in order to prevent the HAPF converter from generating voltage components at fundamental frequency. The *d*-axis component of the reference current signal computed earlier is then combined with the output of the dc-link regulation block, which tends to keep the dc-link voltage v_{dc} at its set value ($V_{\mathrm{dc(set)}}$) by allowing the required amount of bidirectional active power flow between the supply and the dc-link capacitor. The resulting reference current signals (i_d^* and i_q^*) are then transformed to the *abc* axis ($i_{\mathrm{fa}}^*, i_{\mathrm{fb}}^*, i_{\mathrm{fc}}^*$) by the back transformation matrix from *dq*0 to *abc* reference frame.

In this study, the simplest form of the hysteresis band control has been applied to the suppression problem of interharmonics and harmonics produced by IMFs, i.e., fixed hysteresis band, fixed sampling rate, and hence changing switching frequency. During the operation of the HAPF system, hysteresis band controller tends to keep the line currents of individual HAPF units within the fixed hysteresis band of reference current signals ($i_{\mathrm{fa}}^* \pm \Delta I, i_{\mathrm{fb}}^* \pm \Delta I, i_{\mathrm{fc}}^* \pm \Delta I$) as illustrated in Fig. 14. In this figure, $\ldots, t_s, t_{s+1}, t_{s+2,} 1/4$ are the sampling instants, T_s the fixed sampling period, T_e the execution time of the controller (all necessary calculations are carried out in T_e by the DSP board), i_{fx} the actual current in analog form in phase x of each HAPF unit, $i_{\mathrm{fx}(s)}$ the digitized actual current sampled at t_s, and $i_{\mathrm{fx}}^*(s)$ the reference value of the HAPF current calculated in T_e just after t_s from the samples collected at t_s. In each sampling period switching signal, S_X for phase *x* of the HAPF converter is determined by the hysteresis band control block according to the following criteria:

If $i_{\mathrm{fx}}(s) > i_{\mathrm{fx}}^*(s) + \Delta I$, then $S_X = 1$
If $i_{\mathrm{fx}}(s) < i_{\mathrm{fx}}^*(s) - \Delta I$, then $S_X = 0$
If $i_{\mathrm{fx}}^*(s) - \Delta I < i_{\mathrm{fx}}(s) < i_{\mathrm{fx}}^*(s) + \Delta I$, then do not change the previous switching pattern.

$i_{\mathrm{fx}(s)}$ is compared with $i_{\mathrm{fx}}^*(s)$ in the *s*th sampling period in view of the criteria given earlier; if a switching pattern change is required, the new switching pattern will be applied in the next sampling period just after the computations are completed. $S_X = 1$ means that the power semiconductor in leg *x* of the upper half of the converter in Fig. 8 should be turned on or

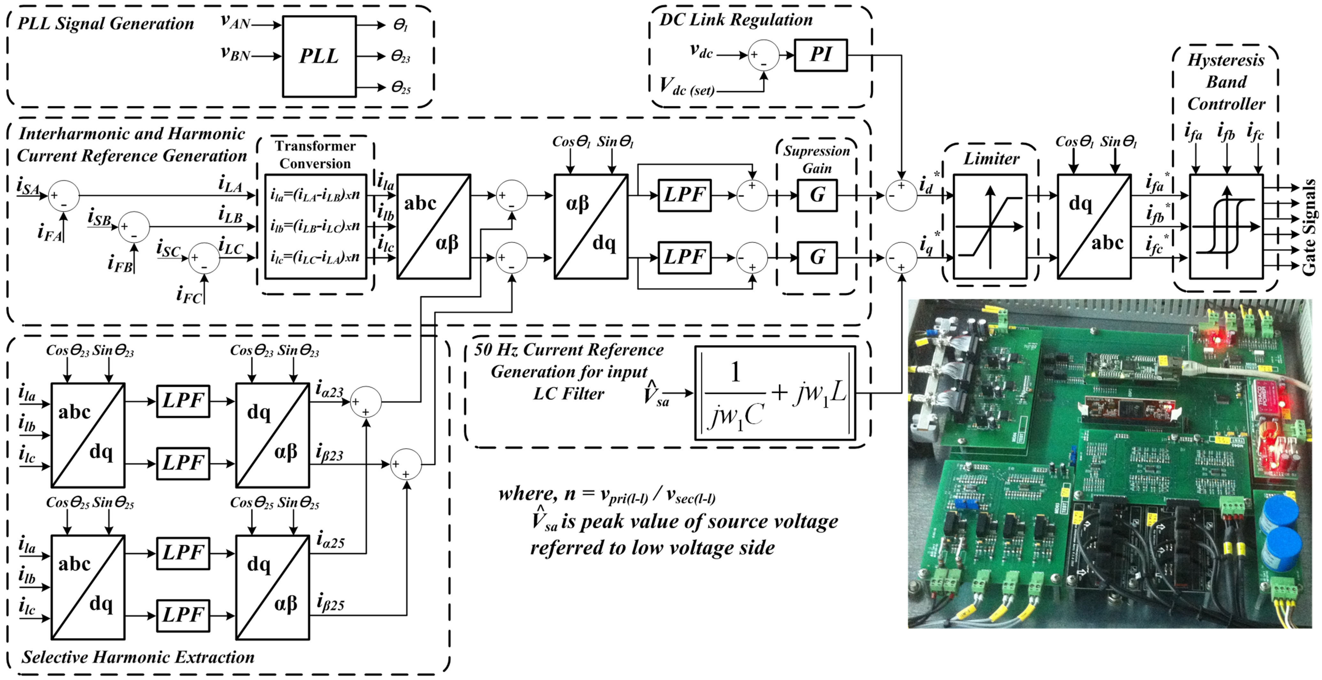

Fig. 13 Block diagram of the control system for each HAPF unit (compact PCB of control system is shown in the background).

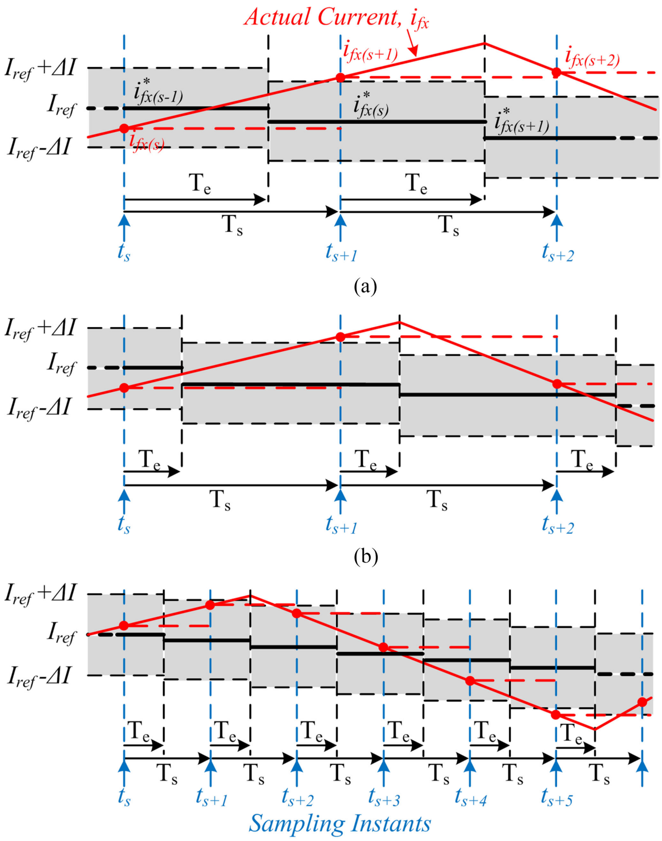

(a)

(b)

(c)

Fig. 14 Illustration for the digital implementation of hysteresis current control (x denotes phase a, b, or c of each HAPF unit in Fig. 13) for (a) the implemented system, (b) a lower execution time T_e, and (c) much lower T_e and sampling period T_s.

should remain in conduction, while the power semiconductor in the same leg of the lower converter half should be turned off or remain in off state. The situation is the same also for the power semiconductor in leg x of the lower half of the converter when $S_X = 0$.

In the implementation of hysteresis current control, sampling rate is 25 kS/s per channel and the $T_e \approx 30\ \mu$s for the chosen DSP board. Suppose that Fig. 14(a) is an illustration of the hysteresis current control implemented in the field. If a more powerful DSP chip were used to reduce the execution time while keeping the sampling rate the same, the response of the hysteresis band controller would be as in Fig. 14(b). Furthermore, the sampling rate could be increased and the execution time could be reduced further by using a more powerful DSP chip. These improvements could yield reference current tracking performance of the control system as illustrated in Fig. 14(c). A comparison of these responses in Fig. 14 shows that the use of high sampling rate and a more powerful digital computing hardware improves the performance of the hysteresis band control at the expense of higher switching frequency by keeping the current variations within the prespecified hysteresis band. Similar findings have already been reported in the literature [39], [40].

Fig. 15 shows all possible switching schemes and the corresponding simplified equivalent circuits for each HAPF unit by assuming an ideal VSC converter. Instantaneous values of source and converter voltages in Fig. 15 are defined with respect to a virtual neutral point. It is at the same potential with the neutral point of the coupling transformer secondary. In order to be able to determine the instantaneous values of converter voltages ($v_{\text{fa}-n}, v_{\text{fb}-n}, v_{\text{fc}-n}$) for all switching schemes, the equivalent circuits in Fig. 15 are to be solved. A sample derivation for the

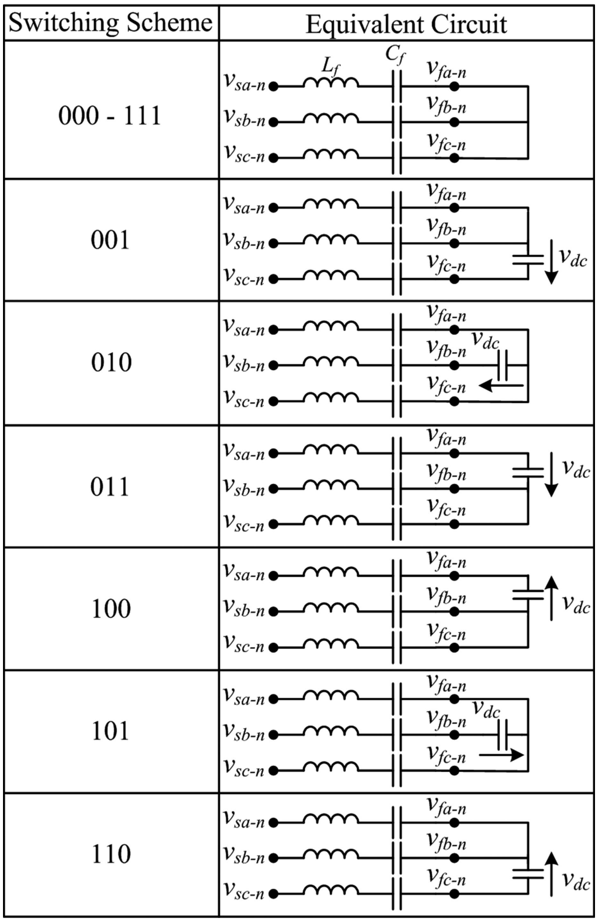

Fig. 15 Possible switching schemes and the corresponding equivalent circuit representations for each HAPF unit.

TABLE II
PHASE VOLTAGES OF EACH HAPF CONVERTER WITH RESPECT TO VIRTUAL NEUTRAL POINT FOR ALL SWITCHING SCHEMES

Switching Scheme	$V_{\mathrm{fa}-n}$	$V_{\mathrm{fb}-n}$	$V_{\mathrm{fc}-n}$
000 - 111	0	0	0
001	$-V_{\mathrm{dc}}/3$	$-V_{\mathrm{dc}}/3$	$2V_{\mathrm{dc}}/3$
010	$-V_{\mathrm{dc}}/3$	$2V_{\mathrm{dc}}/3$	$-V_{\mathrm{dc}}/3$
011	$-2V_{\mathrm{dc}}/3$	$V_{\mathrm{dc}}/3$	$V_{\mathrm{dc}}/3$
100	$2V_{\mathrm{dc}}/3$	$-V_{\mathrm{dc}}/3$	$-V_{\mathrm{dc}}/3$
101	$V_{\mathrm{dc}}/3$	$-2V_{\mathrm{dc}}/3$	$V_{\mathrm{dc}}/3$
110	$V_{\mathrm{dc}}/3$	$V_{\mathrm{dc}}/3$	$-2V_{\mathrm{dc}}/3$

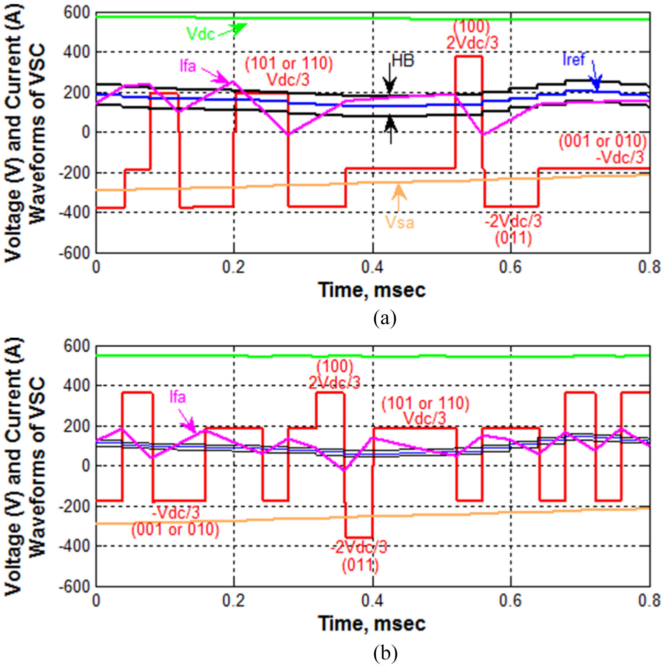

(a)

(b)

Fig. 16 Voltage and current waveforms for each VSC with (a) HB $= 2\Delta I =$ 100 A and (b) HB $= 2\Delta I =$ 30 A (EMTDC/PSCAD simulation results).

Fig. 17 Developed HAPF system, front view of a typical HAPF unit on the left, and rear view showing control PCBs and cooling water piping on the right.

switching scheme of "001" is given in the Appendix. Similar derivations yield line-to-neutral voltages of all phases as given in Table II for all possible eight switching schemes.

The design of the HAPF system is achieved by the aid of a detailed EMTDC/PSCAD model of the overall system in Fig. 3 by using the supply voltage and load current waveforms recorded in the field. This model includes also VSC converters with ideal power semiconductors and the controller software in FORTRAN code. Some instantaneous voltage and current waveforms for one of the VSC converters are as shown in Fig. 16 for two different set values of hysteresis band (HB). These waveforms have been obtained for 1 μs solution time step and 40 μs fixed sampling period, and then PSCAD records are plotted by using MATLAB. These waveforms are consistent with the values in Table II and show that the use of a lower ΔI value yields a better tracking of I_{ref} at the expense of a higher switching frequency.

IV. FIELD PERFORMANCE

Some views of the HAPF system implemented in the field are as given in Fig. 17. Fig. 18 shows interharmonic and harmonic current spectra of line current waveforms of all loads [see Fig. 18(a)] and filtered line current waveforms of the sample steel melt shop [see Fig. 18(b)] on 31.5-kV side for a typical

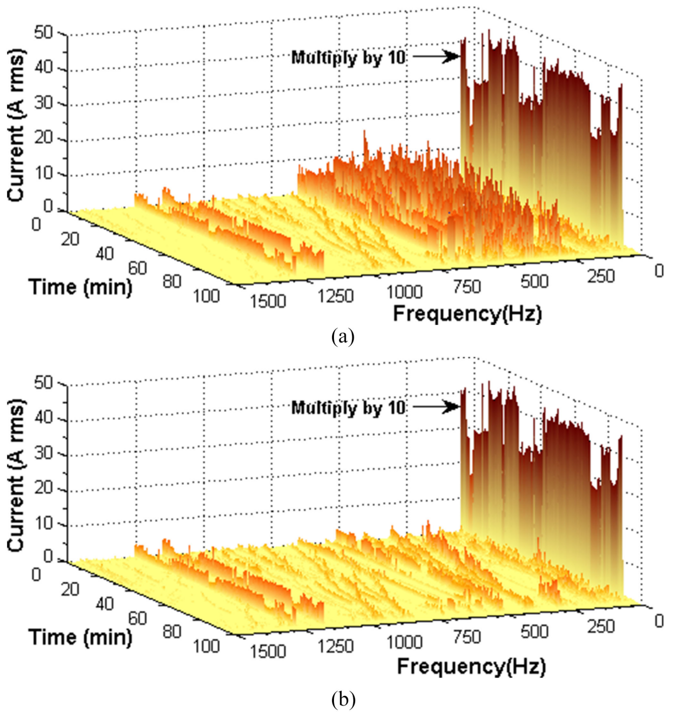

(a)

(b)

Fig. 18 Frequency spectrum of interharmonics and harmonics of the sample steel melt shop containing three IMFs and the HAPF system: (a) the line current waveform of all loads and (b) supply line current waveform.

melting period, while three medium-frequency coreless IMF installations are in operation. As can be understood from Fig. 18, the HAPF system described in this paper successfully suppresses all interharmonics and harmonics excluding 23rd and 25th characteristic current harmonics.

Simultaneously recorded samples of load, HAPF system, and source current waveforms on the MV side and their interharmonic and harmonic spectra with 5 Hz resolution (ten-cycle window) are given in Fig. 19 when three IMFs are in operation. During the sampling period, operating frequencies of load-resonant converters of IMF1, IMF2, and IMF3 are, respectively, 200, 207, and 219 Hz. The corresponding dominant interharmonic current components are (−350 Hz, +450 Hz), (−365 Hz, +465 Hz), and (−388 Hz, +488 Hz), respectively, for IMF1, IMF2, and IMF3. These dominant interharmonics are apparent from Fig. 19(b) and can be related to (1) with negative frequencies corresponding to negative-sequence current components and positive ones to positive sequence. In the recording period, IMF1 produces negative-sequence seventh and positive-sequence ninth harmonic components. These are not characteristic or uncharacteristic power system harmonics given in Table I but arise from cross-modulation phenomenon in the ac–dc–ac link. Total demand distortion (TDD) values of load and source current waveforms in Fig. 19 are calculated by taking into account all line interharmonic and harmonic current components (with 5 Hz resolution) and marked on the associated figures.

Since the fixed sampling frequency used in the implementation of the control system is $1/T_s = 25$ kHz, maximum switching frequency of power semiconductors can be 12.5 kHz. In order to investigate the effects of high-order characteristic power system harmonics and switching frequency and its side bands on the performance of the HAPF system, harmonic spectra of load, HAPF, and source current waveforms in Fig. 19 are replotted in Fig. 20 over the extended frequency range. Since the switching frequency (in the range from 3 to 5 kHz) is much lower than the maximum possible value of 12.5 kHz for $\Delta I = 30$ A, the HAPF system makes negligibly small contribution in the suppression of 23rd, 25th, 35th, and 37th characteristic harmonic components. Furthermore, switching frequency has negligible effects on the line current waveforms on the supply side of the HAPF system.

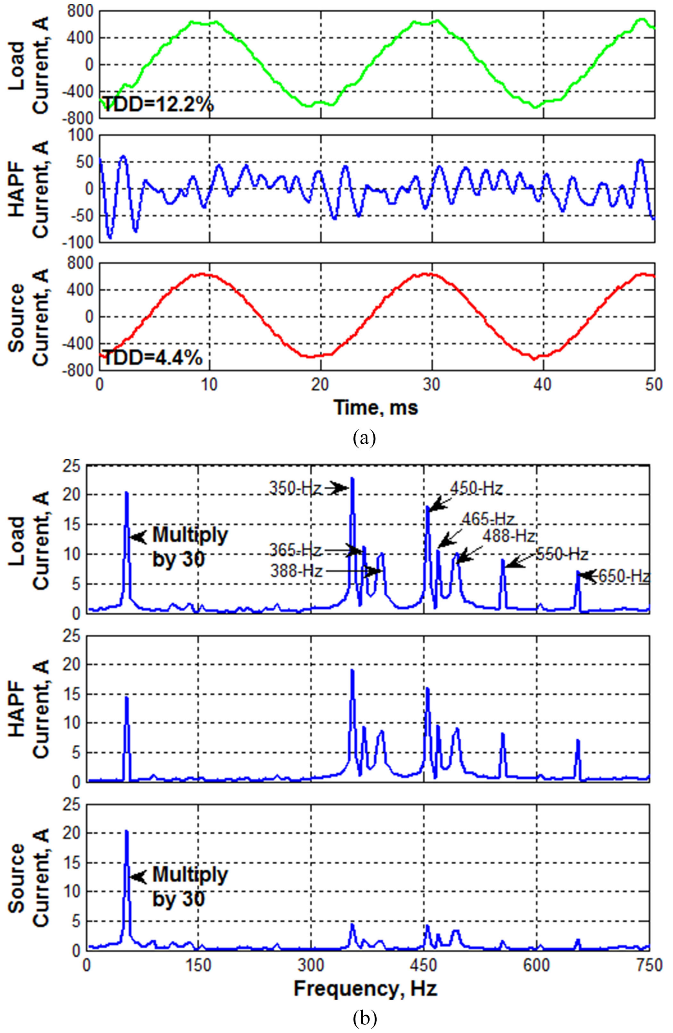

(a)

(b)

Fig. 19 Sample field data deduced from the data recorded on the MV side by Multipurpose platform when three IMFs are simultaneously in operation: (a) current waveforms and (b) harmonic spectra with 5 Hz resolution.

In order to illustrate the success of the implemented hysteresis current control, a sample line current waveform of one of the HAPF units is recorded by a digital storage oscilloscope for a period of 200 ms when two IMFs are in operation. A 20-ms waveform sample is given in Fig. 21(a). The chosen fixed hysteresis band (± $\Delta I = \pm 30$ A) is shown to be marked on the sample current waveform in Fig. 21(b). Frequency spectrum of line

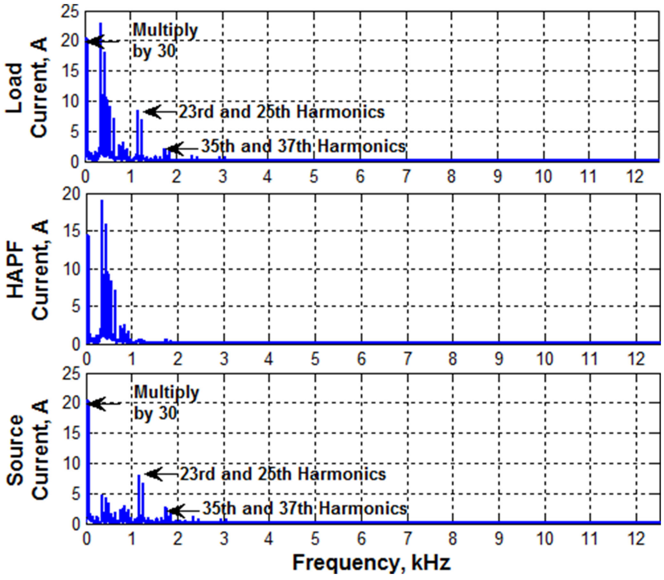

Fig. 20 Harmonic spectra of current waveforms in Fig. 19.

current waveform of the HAPF unit and its extended frequency version are as shown in Fig. 21(c) and (d), respectively. In the current recording period, interharmonic components changing at 330 and 430 Hz are produced by one of the IMF installations operating at 190 Hz. On the other hand, interharmonics at 315 and 415 Hz are produced by the second IMF installation operating at 182.5 Hz. Furthermore, 550 and 650 Hz harmonic current components are also injected by each HAPF unit in order to suppress 11th and 13th characteristic harmonics produced by the 12-pulse IMF installations, as shown in Fig. 21(c). Effects of high-frequency switching arising from hysteresis band control on the frequency spectrum of line current waveform of each HAPF unit are marked on Fig. 21(d).

Field performance of the HAPF system recommended for the suppression of interharmonics and harmonics whose frequencies are varying in the range from 250 to 650 Hz can be quantified by using the suppression factor concept. The percentage value of suppression factor corresponding to each harmonic or interharmonic frequency can be determined as follows:

$$\%\text{Supression Factor}_h = \frac{|I_{h,\text{load}}| - |I_{h,\text{source}}|}{|I_{h,\text{HAPF}}|} \times 100. \quad (4)$$

Percentage suppression factor of 100% stands for the perfect suppression of interharmonic or harmonic current component under evaluation. This does not mean that those interharmonics or harmonics are fully filtered out by the HAPF system. This only tells us that the HAPF system injects the required interharmonic or harmonic current component nearly in correct phase (in anti-phase) with the associated load current component. Furthermore, if the magnitude of the current component injected by the HAPF system were equal to the associated load current component, the associated interharmonic or harmonic component would be eliminated. Obviously, this requires a higher installed capacity and, hence, a costlier HAPF installation.

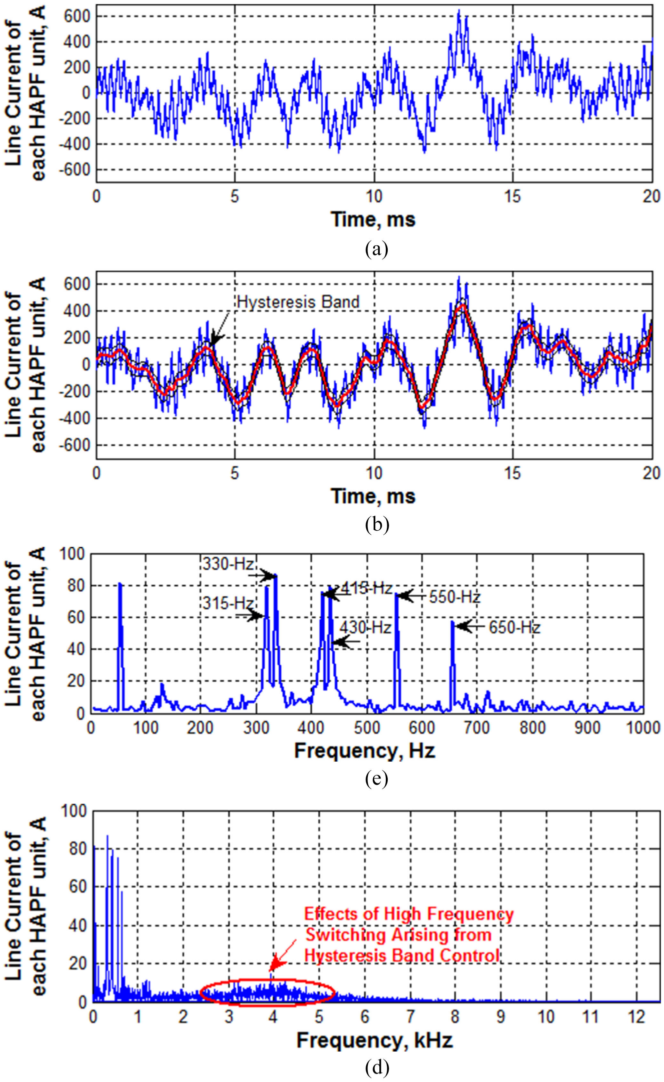

(a)

(b)

(e)

(d)

Fig. 21 Sample line current waveform of one of the HAPF units recorded by digital storage oscilloscope at 25 MS/s for a period of 200 ms when two IMFs are simultaneously in operation: (a) 20 ms current sample, (b) hysteresis band marked on the current sample, (c) frequency spectrum from 0 to 1000 Hz, and (d) frequency spectrum from 0 to 12.5 kHz.

Cloud diagram of suppression factor arising from the recommended hysteresis current control method is given in Fig. 22. For this purpose, a 3-h line current data are recorded in the field by using the multipurpose platform. Line current data sets for the source, load, and HAPF are then expanded into Fourier series by using 200-ms windows. By considering all interharmonics and harmonics in the frequency range from 250 to 650 Hz, suppression factors are separately calculated at time instants $t = 200, 400, \ldots, 3 \times 60 \times 60 \times 1000$ ms, and then marked on Fig. 22. As can be understood from the cloud diagram, the recommended HAPF system and applied hysteresis current control method provides nearly perfect suppression of interharmonic and harmonic frequencies in the frequency range from 250 to 550 Hz. The fifth current harmonic component, which is mainly produced by conventional loads operating in the sample steel melt shop is also suppressed significantly. Eleventh and 13th harmonics are

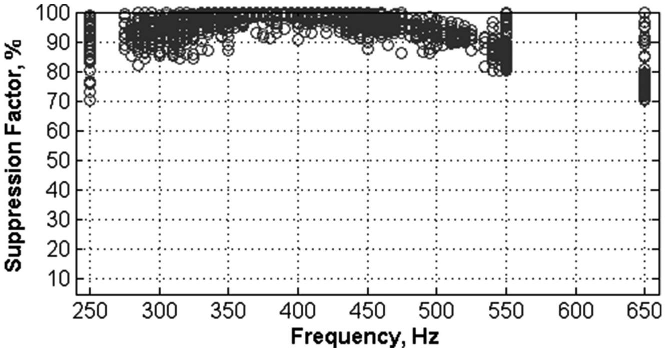

Fig. 22 Cloud diagram of suppression factor arising from the recommended control method (field performance).

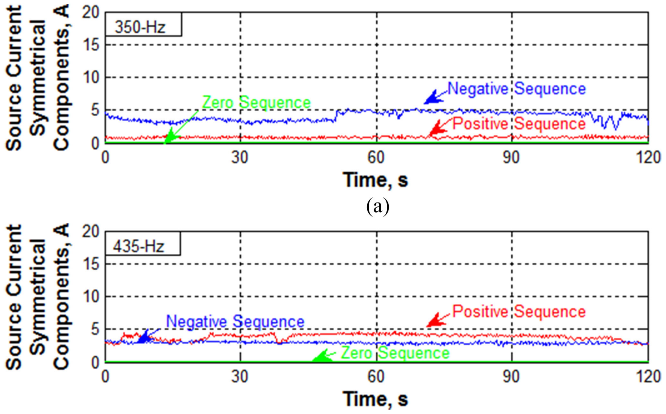

(a)

(b)

Fig. 23 Sequence components of some sample harmonic and interharmonic source current components corresponding to Fig. 7 during the operation of HAPF system (a) $f_h = 350\,\text{Hz}$ and (b) $f_{\text{ih}} = 435\,\text{Hz}$.

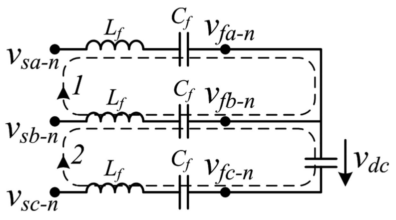

Fig. 24 Equivalent circuit for the switching scheme of "001."

mainly produced by 12-pulse rectifiers. The recommended system significantly reduces the 11th harmonic component while reduction in 13th harmonic is considerable.

The HAPF system described in this paper also reduces significantly negative- and positive-sequence components of all interharmonics and harmonics in the range from 250 to 650 Hz, thereby making the sample steel melt shop nearly a symmetrical load. Some sample field records are given in Fig. 23, which correspond to variations of positive- and negative-sequence components given in Fig. 7.

V. CONCLUSION

The sample medium-power steel melt shop containing 12- and 24-pulse medium-frequency coreless IMF installations is identified by field measurements as a balanced but asymmetrical three-phase three-wire industrial plant. These IMF installations inject interharmonic and harmonic current components into the grid. As the operating frequency of load-resonant inverters supplying work coils is varied from 150 to 250 Hz, frequencies of interharmonics are migrating in time owing to cross-modulation phenomenon in the ac–dc–ac link. These interharmonics may cause dangerous effects on other equipment, especially on reactive power compensation systems, in the sample steel melt shop and the neighboring plants. In this study, these are suppressed satisfactorily by a specially designed HAPF system with hysteresis current control. Field test results show that the resulting HAPF system satisfactorily suppresses all interharmonics and harmonics in the frequency range from 250 to 650 Hz. However, this system is not effective in the suppression of 23rd and 25th characteristic harmonics produced by 12- and 24-pulse thyristor rectifiers. There are no dominant interharmonics between 13th and 23rd harmonics. The magnitudes of 23rd and 25th harmonic current components can also be reduced by applying one of the following counter measures: 1) Hysteresis band in the control system can be set to a value much lower than the one used in the implementation. This is at the expense of a derated use of all HAPF units due to a higher switching frequency and operation at a higher dc-link voltage, or 2) a damped shunt *LC* filter can be connected to the grid bus tuned to an optimum point between 23rd and 25th harmonic frequencies.

APPENDIX

Phase voltages of each HAPF converter with respect to virtual neutral point for all switching schemes can be determined by solving the equivalent circuits in Fig. 15. A sample derivation from the equivalent circuit in Fig. 24 is given later for the switching scheme "001."

The KVL equations for loop 1 and loop 2 are given in (5) and (6), respectively

$$\begin{aligned} v_{\text{sa}-n} - L_f \frac{di_{\text{fa}}}{dt} - \frac{\int i_{\text{fa}}\, dt}{C_f} - v_{\text{Coa}} \\ = v_{\text{sb}-n} - L_f \frac{di_{\text{fb}}}{dt} - \frac{\int i_{\text{fb}}\, dt}{C_f} - v_{\text{Cob}} \end{aligned} \tag{5}$$

$$\begin{aligned} v_{\text{sc}-n} - \frac{L_f\, di_{\text{fc}}}{dt} - \frac{\int i_{\text{fc}}\, dt}{C_f} - v_{\text{Coc}} - v_{\text{dc}} \\ = v_{\text{sb}-n} - \frac{L_f\, di_{\text{fb}}}{dt} - \frac{\int i_{\text{fb}}\, dt}{C_f} - v_{\text{Cob}} \end{aligned} \tag{6}$$

where $v_{\text{Coa}}, v_{\text{Cob}}$, and v_{Coc} are the initial voltages across the series filter capacitors C_f and n denotes the virtual neutral point, which can be taken as the neutral point of the coupling transformer secondary. Since the three-phase, three-wire HAPF units are balanced, (7) and (8) hold

$$i_{\mathrm{fa}} + i_{\mathrm{fb}} + i_{\mathrm{fc}} = 0 \tag{7}$$

$$v_{\mathrm{sa}-n} + v_{\mathrm{sb}-n} + v_{\mathrm{sc}-n} = 0. \tag{8}$$

HAPF converter voltages $v_{\mathrm{fa}-n}, v_{\mathrm{fb}-n}$, and $v_{\mathrm{fc}-n}$ can be related to coupling transformer secondary voltages $v_{\mathrm{sa}-n}, v_{\mathrm{sb}-n}$, and $v_{\mathrm{sc}-n}$ as given in (9)–(11)

$$v_{\mathrm{sa}-n} - L_f \frac{di_{\mathrm{fa}}}{dt} - \frac{\int i_{\mathrm{fa}} dt}{C_f} - v_{\mathrm{Coa}} = v_{\mathrm{fa}-n} \tag{9}$$

$$v_{\mathrm{sb}-n} - L_f \frac{di_{\mathrm{fb}}}{dt} - \frac{\int i_{\mathrm{fb}} dt}{C_f} - v_{\mathrm{Cob}} = v_{\mathrm{fb}-n} \tag{10}$$

$$v_{\mathrm{sc}-n} - L_f \frac{di_{\mathrm{fc}}}{dt} - \frac{\int i_{\mathrm{fc}} dt}{C_f} - v_{\mathrm{Coc}} = v_{\mathrm{fc}-n}. \tag{11}$$

Equation (12) can then be obtained from (5) to (8)

$$-3v_{\mathrm{sb}-n} + 3L_f \frac{di_{\mathrm{fb}}}{dt} + \frac{3\int i_{\mathrm{fb}} dt}{C_f} + 2v_{\mathrm{Cob}} - v_{\mathrm{Coa}} - v_{\mathrm{Coc}}$$
$$-v_{\mathrm{dc}} = 0. \tag{12}$$

Substitution of (10) into (12) gives (13). By rearranging (13), (14) is obtained

$$-3v_{\mathrm{fb}-n} - v_{\mathrm{Coa}} - v_{\mathrm{Cob}} - v_{\mathrm{Coc}} - v_{\mathrm{dc}} = 0 \tag{13}$$

$$v_{\mathrm{fb}-n} = -\frac{v_{\mathrm{dc}}}{3} - \frac{v_{\mathrm{Coa}} + v_{\mathrm{Cob}} + v_{\mathrm{Coc}}}{3}. \tag{14}$$

Summing up (9)–(11) and then using (8) yield (15)

$$v_{\mathrm{Coa}} + v_{\mathrm{Cob}} + v_{\mathrm{Coc}} = -\left(v_{\mathrm{fa}-n} + v_{\mathrm{fb}-n} + v_{\mathrm{fc}-n}\right). \tag{15}$$

Since the right-hand side of (15) is either always zero or decays rapidly to zero, as shown in Fig. 9, (14) reduces to (16)

$$v_{\mathrm{fb}-n} = -\frac{v_{\mathrm{dc}}}{3}. \tag{16}$$

Since $v_{\mathrm{fa}-n} = v_{\mathrm{fb}-n}$ and $v_{\mathrm{fc}-n} = v_{\mathrm{fb}-n} + v_{\mathrm{dc}}$ on equivalent circuit in Fig. 24, (17) and (18) can directly be obtained from (16)

$$v_{\mathrm{fa}-n} = -\frac{v_{\mathrm{dc}}}{3} \tag{17}$$

$$v_{\mathrm{fc}-n} = +\frac{2v_{\mathrm{dc}}}{3}. \tag{18}$$

By repeating the aforementioned derivation for all possible switching schemes, line-to-neutral voltage values given in Table II are obtained. Since only one of the switching schemes is applied in each very short sampling period of 40 μs, line-to-neutral voltages of transformer secondary and HAPF converter and dc-link voltage can be approximated by dc-level voltages, as can be understood from Fig. 16.

ACKNOWLEDGMENT

The HAPF system has been designed and developed by the Power Electronics Department, Tubitak Uzay Institute, Ankara, Turkey (now linked to TUBITAK MAM Energy Institute) for Mega Metallurgy Co. İskenderun, Turkey.

REFERENCES

[1] E. J. Davies and P. G. Simpson, "Induction heating for industry," *Electron. Power*, pp. 508–515, Jul. 1979.

[2] C. J. Edgerley, L. Smith, and C. F. Wilford, "Electric metal melting-a review," *Power Eng. J.*, pp. 83–92, Mar. 1988.

[3] F. P. Dawson and P. Jain, "A comparison of load commutated inverter systems for induction heating and melting applications," *IEEE Trans Power Electron.*, vol. 6, no. 3, pp. 430–441, Jul. 1991.

[4] I. Yilmaz, M. Ermis, and I. Cadirci, "Medium-frequency induction melting furnace as a load on the power system," *IEEE Trans. Ind. Appl.*, vol. 48, no. 4, pp. 1203–1214, Jul.–Aug. 2012.

[5] A. Testa, M. F. Akram, R. Burch, G. Carpinelli, G. Chang, V. Dinavahi, C. Hatziadoniu, W. M. Grady, E. Gunther, M. Halpin, P. Lehn, Y. Liu, R. Langella, M. Lowenstein, A. Medina, T. Ortmeyer, S. Ranade, P. Ribeiro, N. Watson, J. Wikston, and W. Xu, "Interharmonics: Theory and modeling," *IEEE Trans. Power Del.*, vol. 22, no. 4, pp. 2335–2348, Oct. 2007.

[6] R. C. Dugan and L. E. Conrad, "Impact of induction furnace interharmonics on distribution systems," in *Proc. 1991 IEEE Transmiss. Distrib. Conf.*, Apr. 11–16, 1999, vol. 2, pp. 791–796.

[7] I. Yilmaz, O. Salor, M. Ermis, and I. Cadirci, "Field-data-based modeling of medium-frequency induction melting furnaces for power quality studies," *IEEE Trans. Ind. Appl.*, vol. 48, no. 4, pp. 1215–1224, Jul.–Aug. 2012.

[8] E. W. Gunther, "Interharmonics-recommended updates to IEEE 519," in *Proc. IEEE Power Eng. Soc. Summer Meeting*, Jul. 25–25, 2002, vol. 2, pp. 950–954.

[9] A. Tan and K. C. Bayindir, "Modeling and analysis of power quality problems caused by coreless induction melting furnace connected to distribution network," *Elect. Eng.*, vol. 96, no. 3, pp. 239–253, Sep. 2014.

[10] S. Puengsungwan, P. Kumhom, K. Chamnongthai, A. Chaisawadi, and R. H. Lasseter, "Harmonic detection for shunt hybrid active filter using adaptive filter," in *Proc. 2004 IEEE Power Eng. Large Eng. Syst. Conf.*, Jul. 28–30, pp. 102–106.

[11] A. K. Unnikrishnan, J. Aby, and J. T. G Subhash, "Three-level converter based active filter for harmonic compensation of 4MW induction furnace," in *Proc. 2007 IEEE Power Electron. Appl. Eur. Conf.*, Sep., pp. 1–7.

[12] M. Salehifar and A. Shoulaie, "Induction furnace compensation using a hybrid active filter," in *Proc. 2009 Int. Conf. IEEE Tech. Postgraduates (TECHPOS)*, Dec., pp. 1–6.

[13] H. Akagi, "Active harmonic filters," *Proc. IEEE*, vol. 93, no. 12, pp. 2128–2141, Dec. 2005.

[14] H. Akagi, S. Srianthumrong, and Y. Tamai, "Comparisons in circuit configuration and filtering performance between hybrid and pure shunt active filters," in *Proc. 38th IAS Annu. Meeting Conf.*, Oct. 12–16, 2003, vol. 2, pp. 1195–1202.

[15] H. Akagi and R. Kondo, "A transformerless hybrid active filter using a three-level pulsewidth modulation (PWM) converter for a medium-voltage motor drive," *IEEE Trans Power Electron.*, vol. 25, no. 6, pp. 1365–1374, Jun. 2010.

[16] W. Tangtheerajaroonwong; T. Hatada, K. Wada, and H. Akagi, "Design and performance of a transformerless shunt hybrid filter integrated into a three-phase diode rectifier," *IEEE Trans Power Electron.*, vol. 22, no. 5, pp. 1882–1889, Sep. 2007.

[17] V. F. Corasaniti, M. B. Barbieri, P. L. Arnera, and M. I. Valla, "Hybrid power filter to enhance power quality in a medium-voltage distribution network," *IEEE Trans Ind. Electron.*, vol. 56, no. 8, pp. 2885–2893, Aug. 2009.

[18] S. Rahmani, A. Hamadi, N. Mendalek, and K. Al-Haddad, "A new control technique for three-phase shunt hybrid power filter," *IEEE Trans Ind. Electron.*, vol. 56, no. 8, pp. 2904–2915, Aug. 2009.

[19] W. Choi, C. Lam; M. Won, and Y. Han, "Analysis of DC-link voltage controls in three-phase four-wire hybrid active power filters," *IEEE Trans Power Electron.*, vol. 28, no. 5, pp. 2180–2191, May 2013.

[20] R. S. Rebeiro and M. N. Uddin, "Performance analysis of an FLC-based online adaptation of both hysteresis and PI controllers for IPMSM drive," *IEEE Trans Ind. Appl.*, vol. 48, no. 1, pp. 12–19, Jan.–Feb. 2012.

[21] V. Ambrozic, G. S. Buja, and R. Menis, "Band-constrained technique for direct torque control of induction motor," *IEEE Trans Ind. Electron.*, vol. 51, no. 4, pp. 776–784, Aug. 2004.

[22] B.-R. Lin, "Analysis of neural and fuzzy-power electronic control," *IEE Proc. Sci. Meas. Technol.*, vol. 144, no. 1, pp. 25–33, Jan. 1997.

[23] B. K. Bose, "An adaptive hysteresis-band current control technique of a voltage-fed PWM inverter for machine drive system," *IEEE Trans Ind. Electron.*, vol. 37, no. 5, pp. 402–408, Oct. 1990

[24] P. Lohia, M. K. Mishra, K. Karthikeyan, and K. Vasudevan, “A Minimally switched control algorithm for three-phase four-leg VSI topology to compensate unbalanced and nonlinear load,” *IEEE Trans Power Electron.*, vol. 23, no. 4, pp. 1935–1944, Jul. 2008.

[25] J. R. Vazquez and P. Salmeron, “Active power filter control using neural network technologies,” *IEE Proc. Electr. Power Appl.*, vol. 150, no. 2, pp. 139–145, Mar. 2003.

[26] L. Malesani, P. Mattavelli, and P. Tomasin, “High-performance hysteresis modulation technique for active filters,” *IEEE Trans Power Electron.*, vol. 12, no. 5, pp. 876–884, Sep. 1997.

[27] S. K. Khadem, M. Basu, and M. F. Conlon, “Harmonic power compensation capacity of shunt active power filter and its relationship with design parameters,” *IET Power Electron.*, vol. 7, no. 2, pp. 418–430, Feb. 2014.

[28] S. Mikkili and A. K. Panda, “Simulation and real-time implementation of shunt active filter id-iq control strategy for mitigation of harmonics with different fuzzy membership functions,” *IET Power Electron.*, vol. 5, no. 9, pp. 1856–1872, Nov. 2012.

[29] C.-S. Lam, M.-C. Wong, and Y.-D. Han, “Hysteresis current control of hybrid active power filters,” *IET Power Electron.*, vol. 5, no. 7, pp. 1175–1187, Aug. 2012.

[30] S. Sasitharan and M. K. Mishra, “Constant switching frequency band controller for dynamic voltage restorer,” *IET Power Electron.*, vol. 3, no. 5, pp. 657–667, Sep. 2010.

[31] A. Ghosh and A. Joshi, “A new approach to load balancing and power factor correction in power distribution system,” *IEEE Trans Power Del.*, vol. 15, no. 1, pp. 417–422, Jan. 2000.

[32] F. Wu, F. Feng, L. Luo, J. Duan, and L. Sun, “Sampling period online adjusting-based hysteresis current control without band with constant switching frequency,” *IEEE Trans Ind. Electron.*, vol. 62, no. 1, pp. 270–277, Jan. 2015.

[33] R. Davoodnezhad, D. G. Holmes, and B. P. McGrath, “A novel three-level hysteresis current regulation strategy for three-phase three-level inverters,” *IEEE Trans Power Electron.*, vol. 29, no. 11, pp. 6100–6109, Nov. 2014.

[34] L. Zhang, B. Gu, J. Dominic, B. Chen, C. Zheng, and J.-S. Lai, “A dead-time compensation method for parabolic current control with improved current tracking and enhanced stability range,” *IEEE Trans. Power Electron.*, vol. 30, no. 7, pp. 3892–3902, Jul. 2015

[35] T. Atalik, I. Cadirci, T. Demirci, M. Ermis, T. Inan, A.S. Kalaycioglu, and O. Salor, “Multipurpose platform for power system monitoring and analysis with sample grid applications,” *IEEE Trans. Instrum. Meas.*, vol. 63, no. 3, pp. 566–582, Mar. 2014.

[36] *Testing and Measurement Techniques-General Guide on Harmonics and Interharmonics Measurements and Instrumentation for Power Supply Systems and Equipment Connected Thereto*, IEC Std. 61000-4-7, 2.0 ed., 2002.

[37] G. Atkinson-Hope, “Relationship between harmonics and symmetrical components,” *Int. J. Eng. Educ.*, vol. 41, no. 2, pp. 93–104, 2004.

[38] C.-S. Lam, X.-X. Cui, W.-H. Choi, M.-C. Wong, and Y.-D. Han, “Minimum inverter capacity design for LC-hybrid active power filters in three-phase four-wire distribution systems,” *IET Power Electron.*, vol. 5, no. 7, pp. 956–968, Aug. 2012.

[39] Z. Zhou and Y. Liu, “Pre-sampled data based prediction control for active power filters,” *Electr. Power Energy Syst.*, vol. 37, pp 13–22, Jan. 2012.

[40] J. Beerten, J. Verveckken, and J. Driesen, “Predictive direct torque control for flux and torque ripple reduction,” *IEEE Trans. Ind. Electron.*, vol. 57, no. 1, pp. 404–412, Jan. 2010.

Emre Durna (S’15) received the B.Sc. degree in electrical and electronics engineering from Orta Doğu Teknik Üniversitesi, Ankara, Turkey, in 2010, where he is currently working toward the Ph.D. degree.

From 2010 to 2015, he was a Researcher in the Power Electronics Department, Space Technologies Research Institute, The Scientific and Technological Research Council of Turkey (TUBITAK), Ankara, where he was involved specifically on the development of active power filters for metal industry. He is currently a Power Electronics Design Engineer at Aselsan Inc., Ankara.

İlker Yılmaz (S’15) received the B.Sc. degree in electrical and electronics engineering from Orta Doğu Teknik Üniversitesi, Ankara, Turkey, in 2008, where he is currently working toward the Ph.D. degree.

From 2008 to 2012, he was a Researcher, and from 2012 to 2014, he was a Senior Researcher in the Power Electronics Department, Space Technologies Research Institute, The Scientific and Technological Research Council of Turkey (TUBITAK), Ankara. He was the Manager of hybrid active power filter projects developed for metal industry. He is currently a Senior Design Engineer at Başarı Energy, Ankara.

Muammer Ermiş (M’99–SM’14) received the B.Sc., M.Sc., and Ph.D. degrees in electrical engineering from Orta Doğu Teknik Üniversitesi (ODTÜ), Ankara, Turkey, in 1972, 1976, and 1982, respectively, and the M.B.A. degree in production management from Ankara Academy of Commercial and Economic Sciences, Ankara, in 1974.

He is currently a Professor of Electrical Engineering in the Department of Electrical and Electronics Engineering, ODTÜ. His current research interest includes electric power quality.

Dr. Ermiş was a recipient of the Overseas Premium Paper Award from the Institution of Electrical Engineers, U.K., in 1992, and the 2000 Committee Prize Paper Award from the Power Systems Engineering Committee of the IEEE Industry Applications Society. He was also a recipient of the 2003 IEEE Power Engineering Society Chapter Outstanding Engineer Award and the Outstanding Paper Award from the Metal Industry Committee of the IEEE Industry Applications Society in 2009.